

Searching for Solar-like Oscillations Using TESS 2-minute Cadence in Southern Ecliptic Hemisphere

YEZHENG FENG,^{1,2} TAO WU,^{2,3,4,5,6,1} HUI-FANG XUE,^{7,8,9} FEIYANG LI,^{2,5} AND JIA-SHU NIU^{1,10,11}

¹*Institute of Theoretical Physics, Shanxi University, Taiyuan 030006, People's Republic of China*

²*Yunnan Observatories, Chinese Academy of Sciences, 396 Yangfangwang, Guandu District, Kunming, 650216, People's Republic of China*

³*Center for Astronomical Mega-Science, Chinese Academy of Sciences, 20A Datun Road, Chaoyang District, Beijing 100012, People's Republic of China*

⁴*Key Laboratory for the Structure and Evolution of Celestial Objects, Chinese Academy of Sciences, 396 Yangfangwang, Guandu District, Kunming 650216, People's Republic of China*

⁵*University of Chinese Academy of Sciences, Beijing 100049, People's Republic of China*

⁶*International Centre of Supernovae, Yunnan Key Laboratory, Kunming 650216, People's Republic of China*

⁷*Department of Physics, Taiyuan Normal University, Jinzhong 030619, People's Republic of China*

⁸*Institute of Computational and Applied Physics, Taiyuan Normal University, Jinzhong 030619, People's Republic of China*

⁹*Shanxi Key Laboratory for Intelligent Optimization Computing and Blockchain Technology, Jinzhong 030619, People's Republic of China*

¹⁰*State Key Laboratory of Quantum Optics Technologies and Devices, Shanxi University, Taiyuan 030006, People's Republic of China*

¹¹*Collaborative Innovation Center of Extreme Optics, Shanxi University, Taiyuan 030006, People's Republic of China*

ABSTRACT

The TESS space mission has generated an extensive collection of light curves, providing a valuable opportunity to search for solar-like oscillations. Numerous studies have utilized TESS observations to search for solar-like oscillations and achieved excellent results. However, the number of oscillators found by the previous works may be incomplete and significantly below the predicted count. Therefore, we employed a novel method to search for solar-like oscillations. In this work, we utilized TESS 2-minute cadence data to identify solar-like oscillators in the southern ecliptic hemisphere, detecting the presence of oscillations by identifying an excess power hump in the spectrum and combining visual inspection. As a result, we identified 10,548 stars exhibiting solar-like oscillations including 2,972 that had not been reported in previous studies. The ν_{\max} and $\Delta\nu$ of oscillators were determined using the fitting and autocorrelation, and the reliability of the $\Delta\nu$ measurements was further evaluated using the Fourier spectrum of the autocorrelation function. Based on this assessment, 4,775 oscillators were classified as having reliable $\Delta\nu$, including 1,920 that have $\Delta\nu$ measured for the first time.

Keywords: Asteroseismology (73) — red giant stars (1372) — light curves (918)

1. INTRODUCTION

Asteroseismology is a powerful tool for probing stellar internal structures and evolutionary stages, enabling precise determination of fundamental stellar parameters such as mass, radius, surface gravity, and age through the oscillation waves that penetrate stellar interior. Solar-like oscillations are pressure mode oscillations excited by stochastic convection in the outer layers of the stellar surface, same to the excitation mechanism of the solar 5-minute oscillations. Solar-like oscillations are hosted by stars with outer convection zones and are therefore prevalent in lower main sequence stars (MS), sub-giants (SG), and stars on the red giant branch (RGB), horizontal branch (HB), and asymptotic giant branch (AGB) (refer to Joshi & Joshi 2015).

Corresponding author: Tao Wu
wutao@ynao.ac.cn

Corresponding author: Jia-Shu Niu
jsniu@sxu.edu.cn

Solar-like oscillators are most commonly studied in the frequency domain, via the observed power spectral density. The signature of solar-like oscillations in power spectral density (PSD) consists of several sharp peaks, often described using Lorentzian functions, at individual mode frequencies. The amplitudes of these peaks are modulated by a roughly Gaussian distribution, the mean of which is ν_{\max} . Each peak corresponds to an individual oscillation mode. The radial dependence of a mode of oscillation is identified with its radial order, n . The horizontal dependence of the oscillation modes is approximated by spherical harmonic functions, and so each overtone is also identified by its angular degree, l . The separation in frequency between modes with the same **angular** degrees l and consecutive **radial** order n for pressure modes is approximately constant, known as the large frequency spacing $\Delta\nu$. **It is worth noting that a complete identification of a mode requires a third quantum number—the azimuthal order m . However, when the frequency resolution is insufficient and the stellar rotation is slow, the m components generally remain degenerate and cannot be individually resolved.** Combined with the effective temperature, stars exhibiting solar-like oscillations can have their parameters such as mass, radius, luminosity, and surface gravity calculated through scaling relations derived from their oscillation characteristics (Kjeldsen & Bedding 1995; Stello et al. 2009; Kallinger et al. 2010a; White et al. 2011; Bellinger et al. 2019; Bellinger 2019).

In the past two decades, thanks to high-precision space telescopes such as CoRoT (Baglin et al. 2006), Kepler (Borucki et al. 2010), and K2 (Howell et al. 2014), over one hundred thousand of solar-like oscillators have been discovered (Hekker et al. 2009; Mosser et al. 2010; Hekker et al. 2011; Huber et al. 2011; Stello et al. 2013; Huber et al. 2014; Mathur et al. 2016; Yu et al. 2016; Stello et al. 2017). The TESS mission (Ricker et al. 2015) launched by NASA in 2018 has provided a wealth of light curves, giving us the opportunity to search for solar-like oscillations across the entire sky. Recently, numerous studies have attempted to search for solar-like oscillators using TESS observations. For instance, Stello et al. (2022) identified approximately 4,500 oscillating red giants within the Kepler field. Hon et al. (2021) employed machine learning techniques to discover 158,000 solar-like oscillators using 30-minute cadence data across the entire TESS field. Hatt et al. (2023) employed a probabilistic approach (see Nielsen et al. 2022) that focuses on SG and MS stars for the detection of solar-like oscillations, identifying 4,177 oscillators in the TESS 2-minute cadence data from observation of Sectors 1 to 46. Zhou et al. (2024) identified 8,651 oscillators by utilizing the autocorrelation function to detect regularly spaced overtone in the spectrum, using 2-minute cadence light curves from Sectors 1 to 60.

Based on a preliminary simulation of the full TESS sky (TESS GI Proposal No. G011188), TESS is expected to detect oscillators in 500,000 red giants (Silva Aguirre et al. 2020), **which is a far larger count than in the aforementioned catalogues.** Although the previous research have yielded significant results, the number of solar-like oscillators identified using TESS data is far below both the projections. Stello et al. (2022) visually inspected spectra from TESS Full Frame Images (FFIs) for more than 8,000 Kepler oscillating red giants and identified oscillations in about 3,000 stars, with $\Delta\nu$ measurable in only $\sim 20\%$ (570 oscillators) of them. **This suggests that methods relying on the regular repeating patterns, such as those used in Hatt et al. (2023) and Zhou et al. (2024), may lead to many oscillators being missed.** Therefore, we aimed to identify a larger number of solar-like oscillators using methods that do not rely on the detection of the large frequency spacing. In this work, we identified the presence of an excess power hump in the spectrum to search for solar-like oscillations, combining visual inspection.

2. PREVIOUS EXPERIENCE

For solar-like oscillations, ν_{\max} and $\Delta\nu$ are related to stellar mass M , radius R , and effective temperature T_{eff} , and expressed as follows (Kjeldsen & Bedding 1995):

$$\Delta\nu \approx \sqrt{\frac{M/M_{\odot}}{(R/R_{\odot})^3}} \Delta\nu_{\odot}, \quad (1)$$

$$\nu_{\max} \approx \frac{M/M_{\odot}}{(R/R_{\odot})^2 \sqrt{T_{\text{eff}}/T_{\text{eff},\odot}}} \nu_{\max,\odot}, \quad (2)$$

where $T_{\text{eff},\odot} = 5777$ K, $\nu_{\max,\odot} = 3120$ μHz , and $\Delta\nu_{\odot} = 134.88$ μHz (Kallinger et al. 2010b; Hekker 2020). Combining with T_{eff} , the stellar mass, radius, and surface gravity can be calculated as follows:

$$\frac{M}{M_{\odot}} \approx \left(\frac{\Delta\nu}{f_{\Delta\nu} \Delta\nu_{\odot}} \right)^{-4} \left(\frac{\nu_{\max}}{f_{\nu_{\max}} \nu_{\max,\odot}} \right)^3 \left(\frac{T_{\text{eff}}}{T_{\text{eff},\odot}} \right)^{3/2}, \quad (3)$$

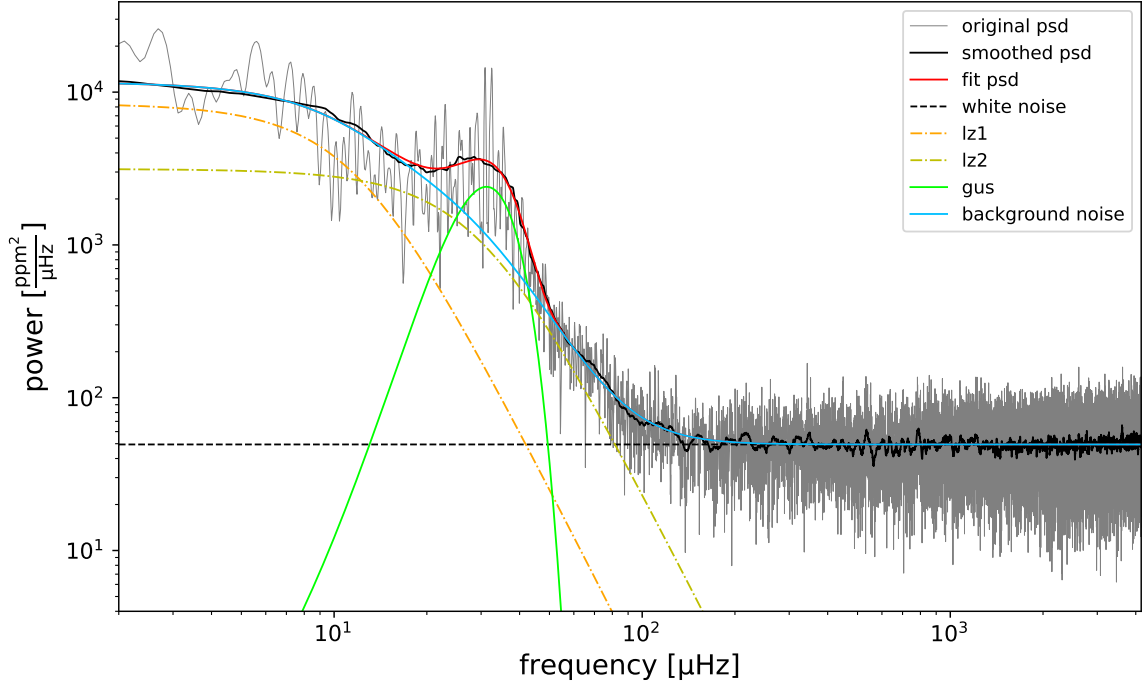


Figure 1. PSD of TIC 469248308. The gray shading represents the original PSD, while the black solid line depicts the median-smoothed PSD with a window width of $4\Delta\nu_{\text{expect}}$. The red solid line illustrates the fit of the smoothed PSD using Equation (7), and the green solid line corresponds to the Gaussian function fitted to the **excess power hump**. The dashed lines in three distinct colors represent the three background noise components, with the blue solid line indicating the total background component.

$$\frac{R}{R_{\odot}} \approx \left(\frac{\Delta\nu}{f_{\Delta\nu}\Delta\nu_{\odot}} \right)^{-2} \left(\frac{\nu_{\text{max}}}{f_{\nu_{\text{max}}}\nu_{\text{max},\odot}} \right) \left(\frac{T_{\text{eff}}}{T_{\text{eff},\odot}} \right)^{1/2}, \quad (4)$$

$$\frac{g}{g_{\odot}} \approx \left(\frac{\nu_{\text{max}}}{f_{\nu_{\text{max}}}\nu_{\text{max},\odot}} \right) \left(\frac{T_{\text{eff}}}{T_{\text{eff},\odot}} \right)^{1/2}, \quad (5)$$

where $f_{\Delta\nu}$ and $f_{\nu_{\text{max}}}$ are correction factors. Different studies have proposed various correction models (Sharma et al. 2016; Hekker 2020; Li et al. 2022; Viani et al. 2017). According to the prescription of Sharma et al. (2016), the correction factors depend on stellar properties such as effective temperature, mass, metallicity, and evolutionary stage.

Hekker et al. (2009) fitted the relationship between ν_{max} and $\Delta\nu$ based on **a sample of red giants** and obtained the following results:

$$\Delta\nu = \Delta\nu_{\odot} \cdot (\nu_{\text{max}}/\nu_{\text{max},\odot})^{0.784 \pm 0.003}. \quad (6)$$

As shown in Figure 1, The PSD of solar-like oscillators can be modeled as the sum of a constant term representing white noise, multiple Lorentzian-like components describing backgrounds varying with frequency (caused by, such as stellar activity, granulation), and a Gaussian function that captures the excess power hump (Harvey 1985; Jiang et al. 2011; Wu et al. 2014). The formula is as follows

$$P(\nu) = P_n + \sum_{i=1}^2 \frac{4\sigma_i^2\tau_i}{1 + (2\pi\nu\tau_i)^2 + (2\pi\nu\tau_i)^4} + D \exp\left(\frac{-(\nu_{\text{max}} - \nu)^2}{2\sigma_g^2}\right), \quad (7)$$

where σ_i is the rms intensity, τ_i is the characteristic timescale, D represents the height at the central frequency of the Gaussian function, and σ_g is the standard deviation of the Gaussian function.

3. TARGET SELECTION

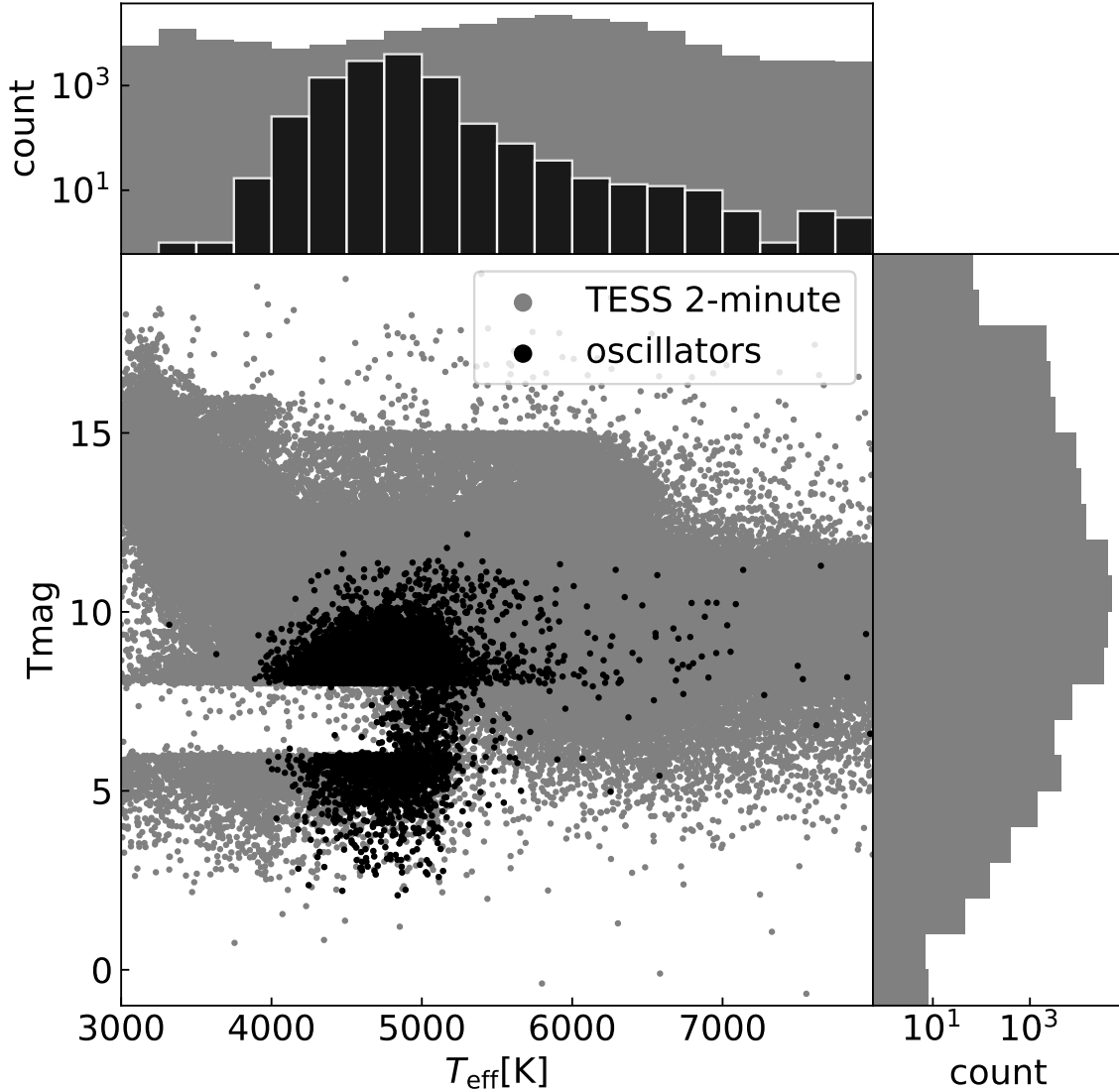


Figure 2. The central panel displays the distribution of sample stars in terms of effective temperature and TESS magnitude. Gray dots represent all target stars, while black dots indicate solar-like oscillators were found in this work. The top panel shows the distribution of stars by T_{eff} , and right panel illustrates the distribution of stars by T_{mag} . Gray shadings represent number of all, **Black shadings** patterns represent number of solar-like oscillators.

105 We selected approximately 220,000 stars observed by TESS with 2-minute cadence in the southern ecliptic hemisphere
 106 during its first and third years (covering Sectors 1 to 13 and 27 to 39¹) as our sample. No additional constraints were
 107 imposed on the stellar parameters.

108 The distribution of these stars in terms of effective temperature T_{eff} and TESS magnitude T_{mag} is illustrated in
 109 Figure 2. As shown in the central panel of Figure 2, there is a marked decline in the number of stars with T_{mag}
 110 between 6 and 8 at temperatures below 5,000 K. This may be due to the target selection criteria of the TESS mission
 111 (Stassun et al. 2018, 2019). The position of the sample on the Hertzsprung–Russell diagram (HRD) is depicted in
 112 Figure 6.

113

4. THE SEARCH PROCESS AND METHODS

¹ https://tess.mit.edu/public/target_lists/target_lists.html

4.1. Obtaining power spectral density

We utilized the Lightkurve² Python package (Lightkurve Collaboration et al. 2018; Astropy Collaboration et al. 2022; Ginsburg et al. 2019) to download the PDC-SAP light curves, which were processed by the TESS Science Processing Operations Center (SPOC) pipeline. For each sector, the light curve was normalized by its median value. The Lomb-Scargle algorithm, which is designed for Fourier transformation in the context of unevenly sampled data (Lomb 1976; Scargle 1982; VanderPlas 2018), was applied to obtain the PSD.

Unlike Kepler, which provided nearly continuous coverage, TESS observes each sector for only 27 days. Owing to the TESS observing strategy, a given target may be covered in multiple sectors, resulting in long gaps in its light curve, which introduce complex sidelobes and affect power value in the PSD. To mitigate these effects, we computed the PSD using the method described by Bedding & Kjeldsen (2022). The PSD was computed by first defining a frequency axis from 2 to 4166 μHz with a step of 0.429/5 μHz . Then, PSDs were calculated for each sector of the same target and then averaged to obtain the final PSD. Here, 4166 μHz represents the Nyquist frequency of the 2-minute cadence, 0.429 μHz corresponds to the frequency resolution for a 27-day observation, and an oversampling factor of 5 was applied.

4.2. Excess power hump fitting

To identify solar-like oscillations through the detection of the excess power hump, it is necessary to characterize the properties of this feature. According to Equation (7), the excess power hump can be modeled by a Gaussian function, whose shape is determined by ν_{max} , D , and σ_g . Therefore, we fitted Equation (7) to the PSDs of 2,749 oscillators detected by Hatt et al. (2023) in the southern hemisphere, allowing us to derive the empirical dependence of D and σ_g on ν_{max} .

The fitting was carried out as follows. The PSD was first smoothed with a moving-average filter using a window of $4\Delta\nu_{\odot} \cdot (\nu_{\text{max}}/\nu_{\text{max},\odot})^{0.784}$ (Hekker et al. 2009). Then, we performed a least-squares fit after taking the logarithm of both Equation (7) and the smoothed PSD. Furthermore, the fit was restricted to frequencies below $2\nu_{\text{max}} + 300 \mu\text{Hz}$, which reduces the computational cost without sacrificing the oscillation features for the fitting. Finally, we visually inspected the fitting results and excluded a small number of stars for which the Gaussian envelope was either not visible in the spectrum or the Gaussian component deviated significantly from the envelope due to the fitting parameters becoming trapped in a local minimum. The distributions of D and σ_g as a function of ν_{max} for the remaining 2,688 stars are shown in Figure 3(a) and 3(b). As shown in the figure, $\log D$ exhibits an approximately linear relation with $\log \nu_{\text{max}}$. However, a slight change in the intercept is observed around $\log \nu_{\text{max}} \approx 2.1$. To account for the fact that the $\nu_{\text{max}}-D$ relation differs for stars in different evolutionary stages, we employed a piecewise linear function with a breakpoint at $\log \nu_{\text{max}} = 2.1$ to fit the relation between $\log D$ and $\log \nu_{\text{max}}$. The resulting fit is indicated by the blue solid line in Figure 3(a):

$$\log D = \begin{cases} (6.81 \pm 0.03) - (2.14 \pm 0.02) \log \nu_{\text{max}}, & \log \nu_{\text{max}} \leq 2.1 \\ (7.64 \pm 0.08) - (2.45 \pm 0.03) \log \nu_{\text{max}}, & \log \nu_{\text{max}} > 2.1 \end{cases} \quad (8)$$

Similarly, $\log \sigma_g$ exhibits an approximately linear dependence on $\log \nu_{\text{max}}$, but with a mild deviation from strict linearity. To capture this trend more accurately, we fitted the relation between $\log \sigma_g$ and $\log \nu_{\text{max}}$ using a fourth-order polynomial. The coefficients from higher-order terms to lower-order terms are 0.142 ± 0.011 , -1.00 ± 0.085 , 2.476 ± 0.243 , -1.697 ± 0.299 , and 0.451 ± 0.133 , respectively. The resulting fit is shown as the blue solid line in Figure 3(b).

We also evaluated the goodness of fit in the vicinity of the excess power hump, defined as the frequency range from $\nu_{\text{max}} - 3\sigma_g$ to $\nu_{\text{max}} + 3\sigma_g$. The formula for calculating the goodness of fit is as follows:

$$R^2 = 1 - \frac{\sum_i (y_i - \hat{y}_i)^2}{\sum_i (y_i - \bar{y})^2}, \quad (9)$$

where y_i represents the observed values, \hat{y}_i denotes the fitted value from model, and \bar{y} is the mean of the observed values. The distribution of the goodness of fit as a function of ν_{max} is shown in Figure 3(c). Although the fitting was performed in logarithmic space, the goodness of fit was evaluated in linear space. As illustrated in Figure 3(c),

² <https://docs.lightkurve.org/index.html>

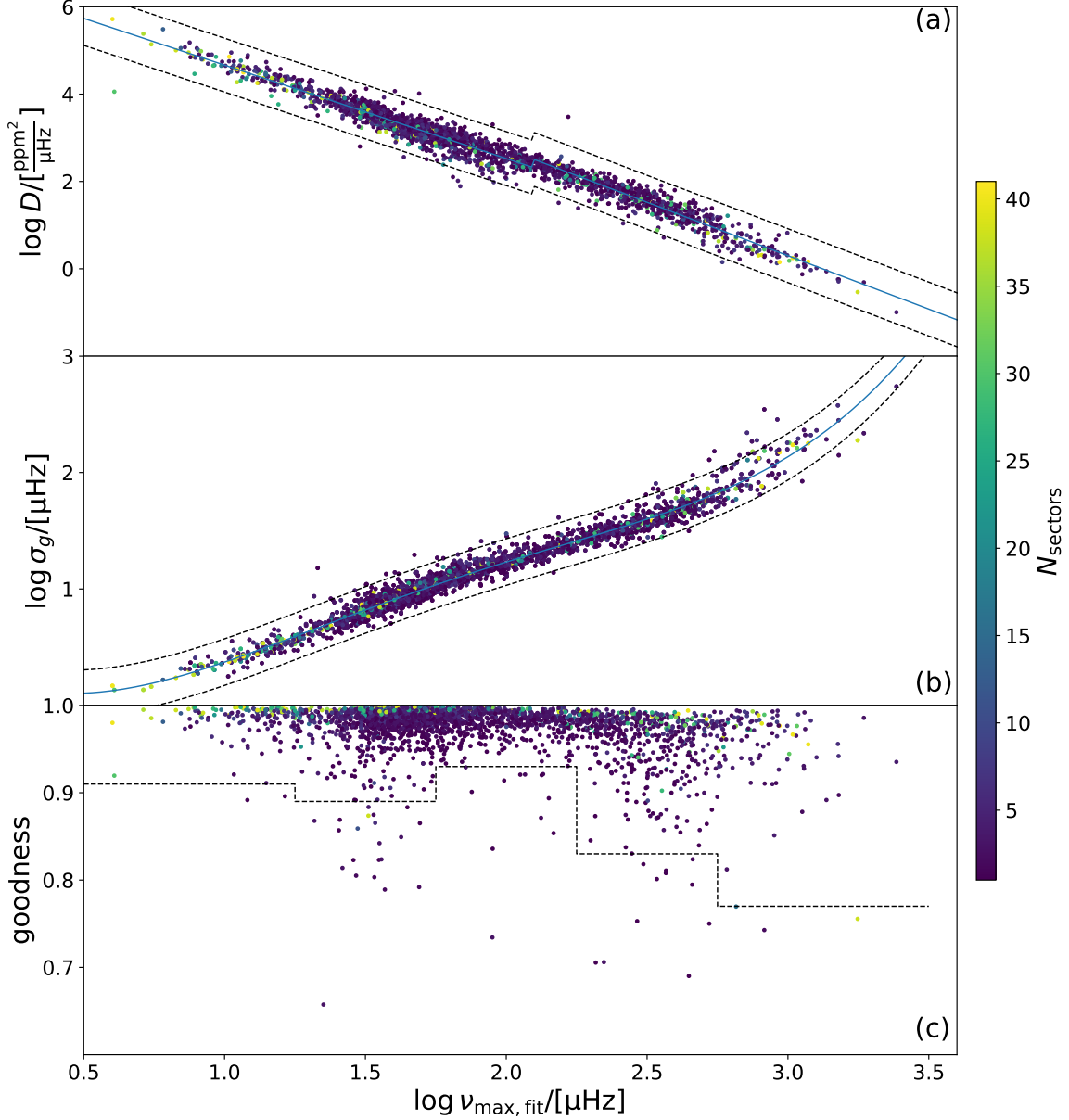


Figure 3. Distributions of $\log D$ (a), $\log \sigma_g$ (b), and the goodness of fit (c) as functions of ν_{\max} . The blue solid lines denote the fitted relations. Dashed lines in panels (a) and (b) indicate the fitted function offset by $\pm 3\sigma$ of the residuals. Dashed line in panel (c) indicates the 2nd percentile of the goodness of fit values within each $\log \nu_{\max}$ interval (98% lie above). **The bin boundaries are 0.5, 1.25, 1.75, 2.25, 2.75, and 3.5.**

157 the majority of the **excess power humps** are well reproduced, indicating that performing the fitting in logarithmic
 158 space is justified.

159 4.3. Search for oscillations

160 In the absence of oscillations or other distinctive signals, the underlying trend of the PSD either decreases or remains
 161 flat with increasing frequency, implying a trend slope ≤ 0 . **Excess power hump** of solar-like oscillations produce a
 162 localized positive slope in this trend. We therefore aim to detect **excess power hump** by identifying such changes in
 163 the slope of the trend of the PSD. Obtaining the underlying trend of a curve by applying a boxcar mean is a common
 164 practice. However, since solar-like oscillations with different ν_{\max} values possess different $\Delta\nu$, extracting the trend

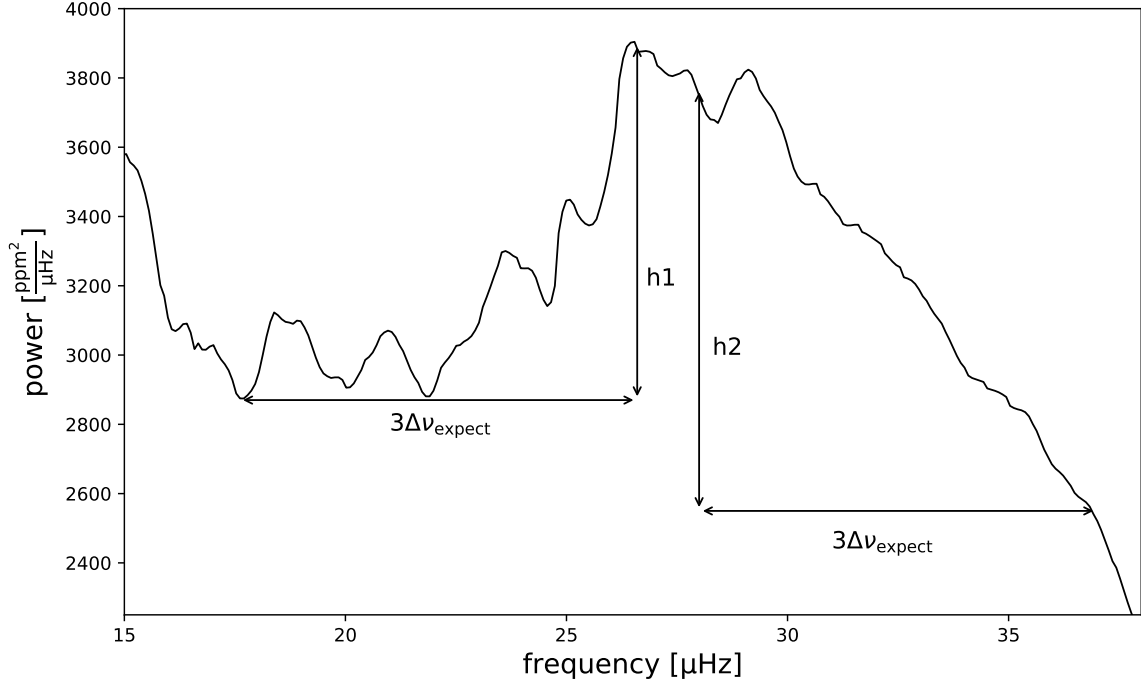


Figure 4. Smoothed PSD of TIC 469248308, where h_1 and h_2 must satisfy Equation (10) and Equation(11) respectively in order to be considered a potential solar-like oscillation.

near the hump requires a smoothing scale that depends on $\Delta\nu$. Therefore, our method applies a running mean with a variable window of $4\Delta\nu_{\odot} \cdot (\nu/\nu_{\max,\odot})^{0.784}$ (denoted $\Delta\nu_{\text{expect}}$) to the PSD, where ν denotes frequency.

Random fluctuations in the smoothed curve, whose amplitude depends on the smoothing window size, prevent the direct detection of the **excess power** hump from the slope. Therefore, we computed the slope of the smoothed PSD between points separated by $3\Delta\nu_{\text{expect}}$, and defined a minimum slope threshold based on the smoothed high-frequency region (only contains a white-noise component). The detailed procedure is outlined as follows. If $p(\nu)$ represents the smoothed PSD, we detect excess power hump by verifying whether $p(\nu)$ satisfies the following two conditions (this process is illustrated in Figure 4):

$$p(\nu_1) - p(\nu_1 - 3\Delta\nu_{\text{expect}}) \geq \text{threshold}, \quad (10)$$

and

$$p(\nu_2) - p(\nu_2 + 3\Delta\nu_{\text{expect}}) \geq \text{threshold}, \quad (11)$$

where $\nu_1 \leq \nu_2$. The threshold was set to 3σ of the smoothed PSD above $3500 \mu\text{Hz}$, where the smoothing used a window size identical to that applied at ν_1 . If ν_1 and ν_2 satisfying the above conditions are present in the smoothed PSD, we consider that the PSD may contain excess power hump of solar-like oscillations.

Not all PSDs satisfying Equations (10) and (11) necessarily correspond to excess power humps from solar-like oscillations; some may arise from other signals or random fluctuations. To verify the nature of these features, we fitted each PSD using $(\nu_1 + \nu_2)/2$ as the initial ν_{\max} , following the same procedure described in Section 4.2. We expect the fitted parameters D and σ_g of genuine solar-like oscillations to follow the distributions of those identified by Figure 3. Hence, PSDs with D and σ_g lying within 3σ of the fitted relations in Figures 3(a) and 3(b) (dashed lines) were classified as possible solar-like oscillators. Additionally, only fits with goodness-of-fit values exceeding the threshold indicated by the dashed line in Figure 3(c) were retained.

The method achieves a detection rate of about 91.5% and a false positive rate of 2.7% when tested on 2,749 oscillators identified by Hatt et al. (2023) in the southern ecliptic hemisphere and 2,000 randomly selected stars from the same region (the detection rates in different ν_{\max} ranges are shown in Figure 5). Increasing the thresholds in Equations (10) and (11) to 4σ reduces the detection rate to 89.2% while lowering the false positive rate to 1.8%.

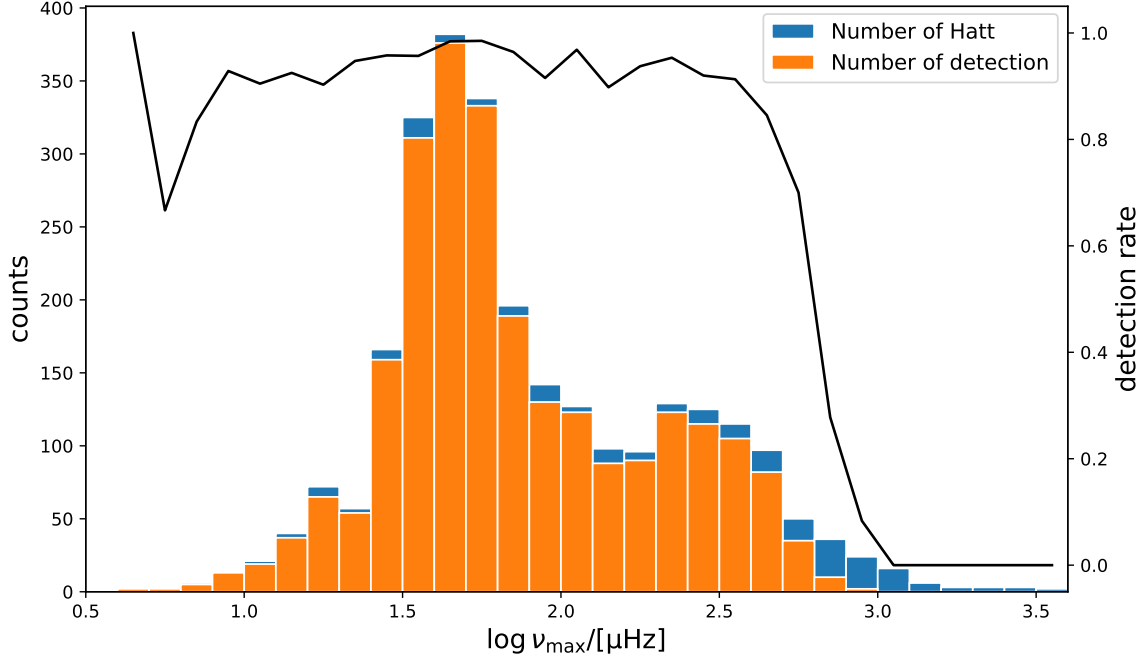


Figure 5. Detection rates in different ν_{\max} intervals. Blue bars denote the number of solar-like oscillators detected by Hatt et al. (2023), orange bars represent those recovered by our method, and the black line shows the detection rate as a function of ν_{\max} .

The method was then applied to the light curves of all 220,000 sample stars, resulting in the identification of 16,800 candidates. Further visual inspection led to the identification of a final set of 10,548 solar-like oscillators. The distribution of these oscillators in the HRD is shown in Figure 6.

5. MEASURING ν_{\max} AND $\Delta\nu$ WITH AUTOCORRELATION

The segmented autocorrelation function (ACF) of spectrum method is employed to measure both ν_{\max} and $\Delta\nu$ (Huber et al. 2009). As described in Section 4.2, we fit oscillation spectrum to obtain the $\nu_{\max, \text{fit}}$ and then use Equation (6) to estimate $\Delta\nu$, denoted as $\Delta\nu_{\text{estimate}}$. We then extract and analyze the oscillation signal within the frequency range of $\nu_{\max, \text{fit}} - 3\sigma_g - 2\Delta\nu_{\text{estimate}}$ to $\nu_{\max, \text{fit}} + 3\sigma_g + 2\Delta\nu_{\text{estimate}}$. As shown in Figure 7, ν_{\max} and $\Delta\nu$ are measured.

As shown in Figure 7(a), we divided the original PSD by the background component. Next, the processed oscillations is divided into overlapping segments represented by its central frequency, each with a length of $4\Delta\nu_{\text{estimate}}$ and a step of $0.1\Delta\nu_{\text{estimate}}$. The ACF for each segment is calculated with spacing ranging from $0.5\Delta\nu_{\text{estimate}}$ to $1.5\Delta\nu_{\text{estimate}}$. This result in a two-dimensional matrix, as shown in Figure 7(b), where each column represents the ACF of a sub-segment. Then, we collapse (normalize after summing) the matrix and absolute values of the matrix along horizontal and vertical axes, respectively. The collapsed results are presented in Figure 7(d) and 7(c). Subsequently, the collapsed result in Figure 7(c) is fitted with a Gaussian function. The value of ν_{\max} was adopted as the center of the fitted Gaussian function. The collapsed result in Figure 7(d) is Gaussian smoothed with $\sigma = 0.05\Delta\nu_{\text{estimate}}$ and the measurement of $\Delta\nu$ was taken as the maximum peak in the range of $0.7\Delta\nu_{\text{estimate}}$ to $1.3\Delta\nu_{\text{estimate}}$.

Following the approach of Huber et al. (2011), we perturb the power spectrum using a χ^2 distribution with two degrees of freedom and recompute ν_{\max} and $\Delta\nu$ for each realization. After 500 iterations, the standard deviations of the resulting distributions are adopted as the uncertainties in ν_{\max} and $\Delta\nu$.

The above method for calculating $\Delta\nu$ always returns a value, but not all solar-like oscillators yield a reliable $\Delta\nu$. Therefore, we assessed the reliability of $\Delta\nu$ using the discrete Fourier transform (DFT) of the autocorrelation function of the oscillation signal (Zhou et al. 2024). According to the asymptotic representation of high-order p modes (Aerts 2021):

$$\nu_{nl} \simeq \left(n + \frac{l}{2} + \frac{1}{4} + \alpha\right)\Delta\nu, \quad (12)$$

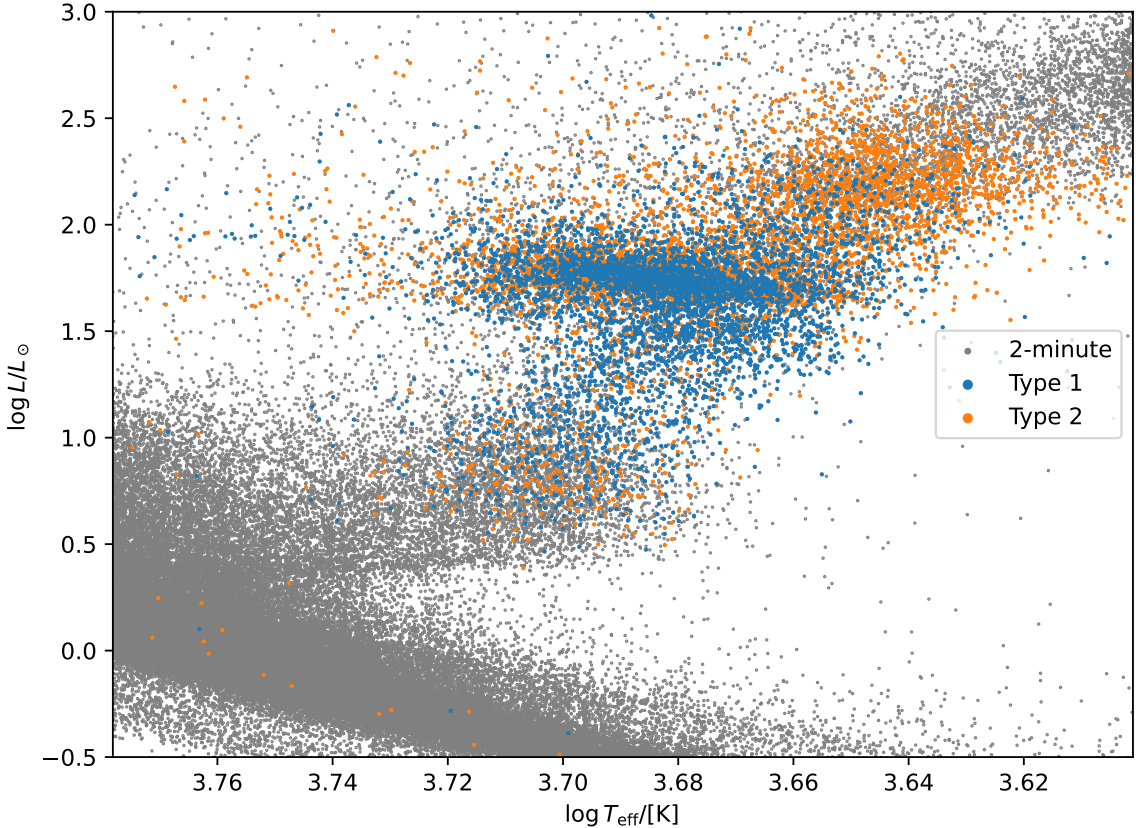


Figure 6. Positions of solar-like oscillators identified in this work on the Hertzsprung-Russell diagram. Gray points represent all sample stars. The blue and orange dots indicate oscillators classified as “type 1” and “type 2”, respectively. The luminosity is estimated using the radius and effective temperature provided in the TESS Input Catalog, based on the Stefan–Boltzmann relation.

216 the ACF of solar-like oscillations exhibits regularly spaced peaks, located at half integer multiples of the large frequency
 217 spacing, as shown in Figure 8 upper panel (Huber et al. 2009). The quasi-periodic signal manifests as a distinct peak
 218 in the frequency domain. According to Parseval’s theorem, the total energy of a signal is conserved between the time
 219 and frequency domains; therefore, the integrated power within a given frequency range reflects the energy associated
 220 with the corresponding periodicity. We thus quantify the reliability of $\Delta\nu$ as the ratio between the integrated power
 221 of the relevant peak in the power spectrum of autocorrelation function and the total integrated power. The procedure
 222 is as follows. First, we compute the autocorrelation function (ACF) of the solar-like oscillation signal (Figure 7(a))
 223 and normalize its horizontal axis by dividing by $\Delta\nu$ (Figure 8). We then remove the long-period trend in the ACF
 224 by performing a linear fit and compute the power spectrum for spacings greater than 0.2 using a Fourier transform.
 225 Subsequently, we identify the highest peaks in the ranges 0.9–1.1 and 1.8–2.2, fit them with two Gaussian functions,
 226 and finally calculate the ratio of the integrated power within 2σ of the fitted Gaussians to the total integrated power.

227 We analyzed 2,694 solar-like oscillators identified by Hatt et al. (2023). Only those stars whose $\Delta\nu$ values agree
 228 with the literature within 10% were considered reliable measurements, resulting in a total of 2,375 stars meeting
 229 this criterion. For these stars, we calculated the ratio as described above (blue points in Figure 9). To construct a
 230 reference sample representing noise backgrounds, we randomly selected 2694 stars from the sample of 220,000 stars
 231 excluding oscillators and fitted their PSDs using a Harvey model without a Gaussian envelope. For each of these
 232 stars, we estimated the signal-to-noise ratio and then injected the ν_{\max} and σ_g values derived from the corresponding
 233 real oscillators to define the same frequency range used in the $\Delta\nu$ measurement. These frequency segments were
 234 subsequently processed through the same $\Delta\nu$ -measuring, yielding a spurious “ $\Delta\nu$ ” for each background star. Finally,
 235 we computed the ratio as described above (red points in Figure 9), to characterize the apparent periodicity in the
 236 noise sample.

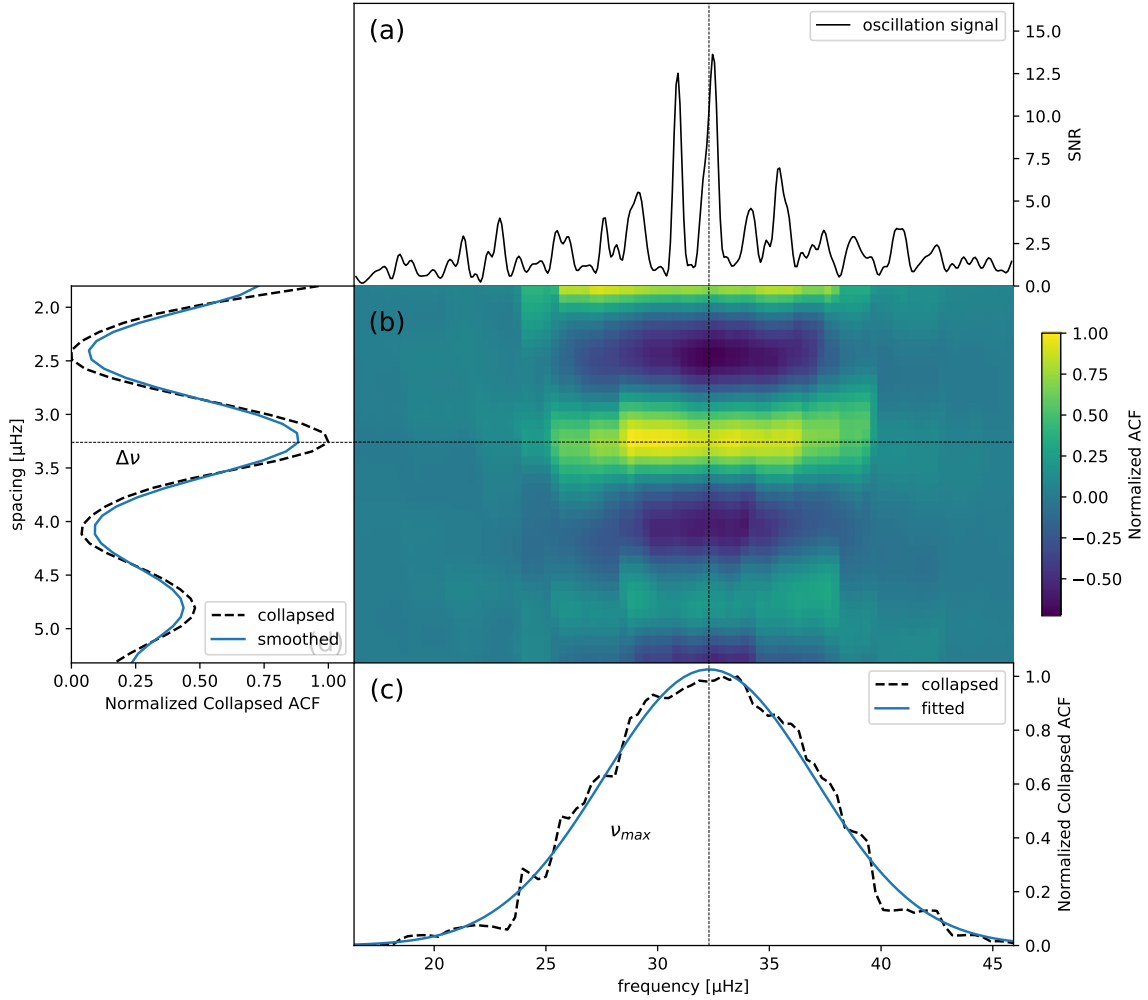


Figure 7. An example measurement of ν_{max} and $\Delta\nu$ is shown for TIC 469248308. In panel (a), the black solid line represents the signal-to-noise ratio obtained by dividing the PSD by the background component. Panel (b) shows the ACF for all segments with each column along the vertical axis representing a sub-segment ACF. Panels (c) and (d) display the results of panel (b) after vertical and horizontal collapsing, respectively. These results have been normalized, with the dashed lines indicating the measured values of ν_{max} and $\Delta\nu$.

As shown in Figure 9, although oscillating and non-oscillating stars cannot be fully separated, their ratio distributions differ markedly. The black solid line indicates the 95th percentile of the ratio distribution for non-oscillating stars. Using this line as the threshold, 1,788 of the 2,375 oscillators lie above it, while 587 fall below it. Oscillators identified in this work above this line are classified as Type 1 ($\Delta\nu$ are considered reliable), while those below are classified as Type 2 ($\Delta\nu$ are considered unreliable). Among the 10,548 oscillating stars identified, 4,775 are labeled as Type 1 and 5,773 as Type 2. The result of measurements are listed in Table 1.

The distributions of the $\Delta\nu$ uncertainties for the Type 1 oscillators and the ν_{max} uncertainties for all oscillators are shown in Figure 10. The curves in different colors represent the uncertainty distributions for stars observed in different numbers of TESS sectors. As shown in the figure, the measurement uncertainties decrease with increasing observing time, a trend that is consistent with the results reported by Zhou et al. (2024).

6. RESULT

6.1. Comparison with Fundamental Stellar Parameters

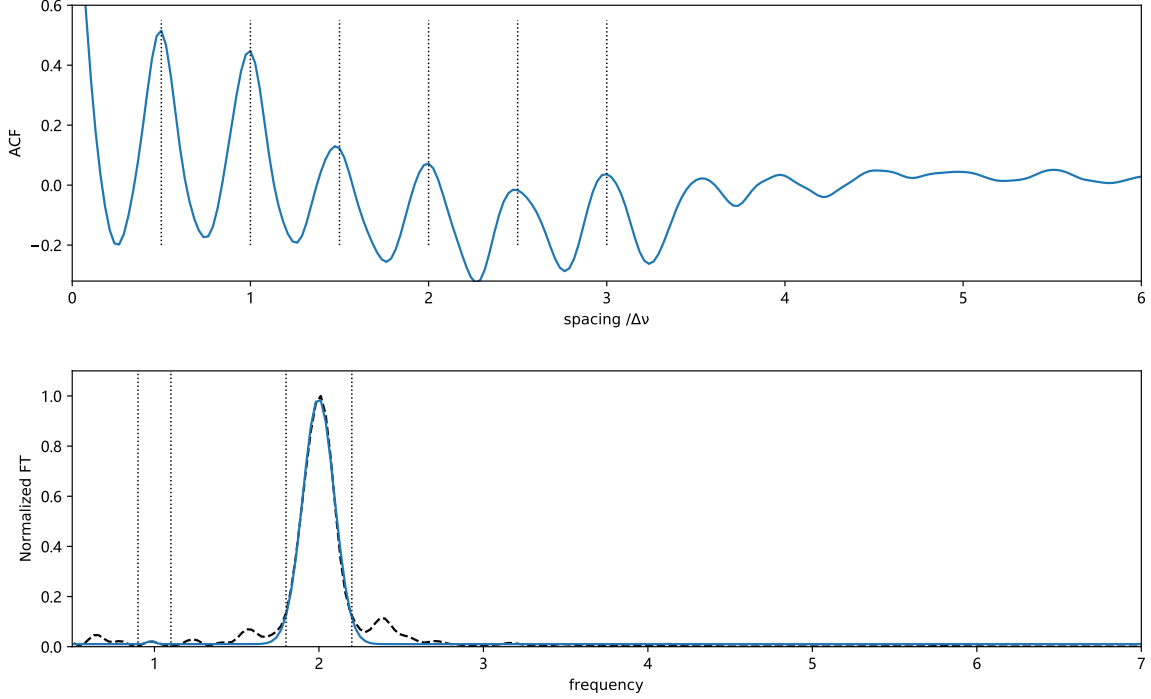


Figure 8. The upper panel displays the autocorrelation function (ACF) of the oscillations for TIC 469248308, and the lower panel shows the Fourier spectrum of the corresponding ACF. The black dashed line in the lower panel shows the normalized power spectrum, and the blue solid line represents its fit.

249 According to Equation (4), stellar radii can be estimated from the solar-like oscillation parameters ν_{\max} , $\Delta\nu$, and
 250 the effective temperature (where we adopt $f_{\Delta\nu} = 1$ and $f_{\nu_{\max}} = 1$). Since the TESS Input Catalog (TIC) (Stassun
 251 et al. 2018, 2019) also provides T_{eff} and stellar radii, we use these catalog values as an external reference to verify
 252 search results in this work. For stars classified as Type 2, their $\Delta\nu$ values are estimated using Equation (6). The
 253 comparison between the asteroseismic radii R_{seis} and the TIC radii R is presented in Figure 11. The lower panel
 254 shows the fractional residuals between the R_{seis} and the R . For stars classified as Type 1 (left panels), the median,
 255 5th percentile, and 95th percentile of the fractional residuals (indicated by the short-dashed and dotted lines) are
 256 9.6%, -6.9% , and 32.2% , respectively. For Type 2 stars (right panels), these values are 7.3% , -21.9% , and 42.9% ,
 257 respectively.

258 For the Type 1 stars, a clear systematic offset is visible. This discrepancy is likely due to the lack of a correction
 259 factor in the asteroseismic radius calculation. Figure 7 of Sharma et al. (2016) provides the correction factor $f_{\Delta\nu}$,
 260 which depends on $[\text{Fe}/\text{H}]$, mass, and evolutionary state. By cross-matching with Gaia, we obtained $[\text{Fe}/\text{H}]$ and mass
 261 for 2,449 Type 1 oscillators. However, we were unable to distinguish between the pre-RGB-tip and post-RGB-tip
 262 evolutionary phases. Since all oscillators in this work have effective temperatures above 4000K, and the correction
 263 factor for post-RGB-tip stars at $T_{\text{eff}} > 4000\text{K}$ is close to unity 1.0, we adopted the pre-RGB-tip correction for all
 264 2,449 stars. The corrected radii are shown as orange points in Figure 10. After applying the correction, the median
 265 fractional residual decreases to 5.8% . However, a systematic offset still remains, suggesting that additional corrections,
 266 such as for ν_{\max} , may be necessary.

267 We also compared the surface gravity derived from Gaia DR3 with that obtained from scaling relations. We used
 268 TOPCAT³ to cross-match positional coordinates within a 1 arcsecond radius to obtain stellar parameters from Gaia
 269 DR3. As a result of the cross-match, we obtained 9,666 oscillators, of which only 5,191 have surface gravity $\log g_{\text{Gaia}}$
 270 (from GSP-Phot). The surface gravity $\log g_{\text{seis}}$ can be also calculated using Equation (5). The comparison between
 271 the $\log g_{\text{seis}}$ and the $\log g_{\text{Gaia}}$ is presented in Figure 12. The lower panel shows the residuals between $\log g_{\text{Gaia}}$ and
 272 $\log g_{\text{seis}}$. For oscillators classified as Type 1 (left panels) the median, 5th percentile, and 95th percentile of the residuals

³ <https://www.star.bris.ac.uk/~mbt/topcat>

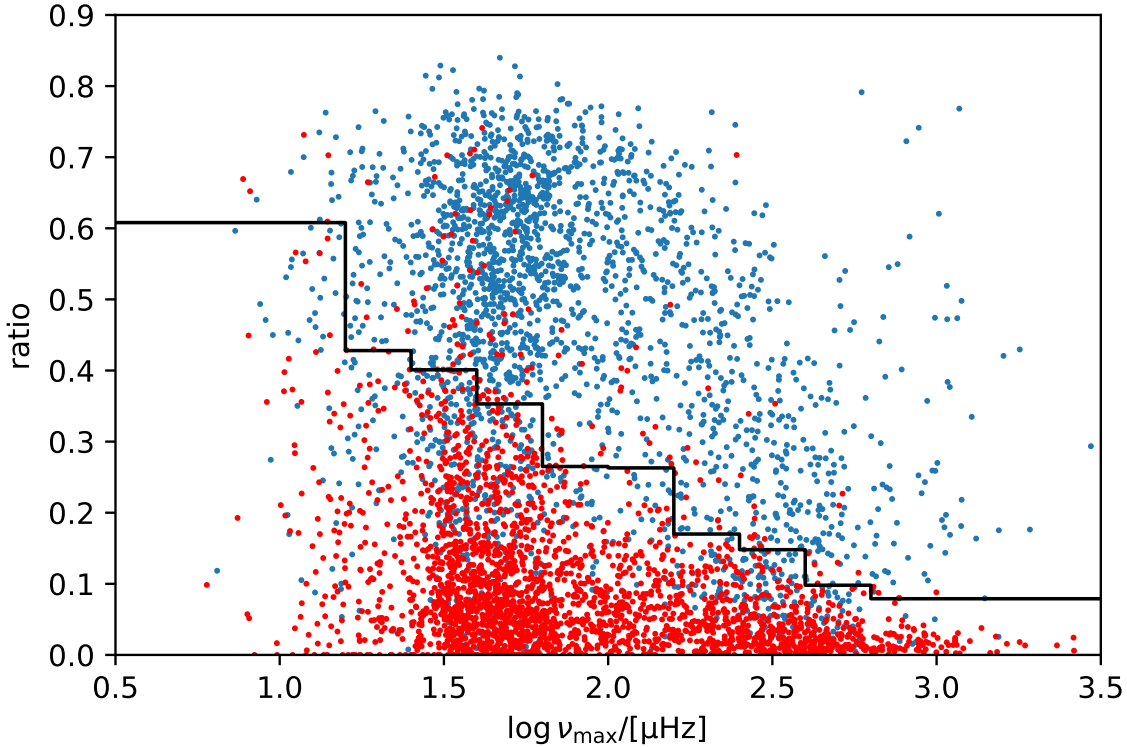


Figure 9. Blue dots represent the ratios (as described in Section 5) of oscillating stars from the literature, while red dots indicate the ratios of non-oscillating stars. The black solid line denotes the 95th percentile of the ratio distribution for non-oscillating stars.

273 are 0.068, -0.289 , and 0.370 , respectively. For Type 2 stars (right panels), these values are 0.151 , -0.256 , and 0.550 ,
 274 respectively. Additionally, as shown in lower panels of Figure 12, a systematic bias is observed between $\log g_{\text{Gaia}}$ and
 275 $\log g_{\text{seis}}$, with $\log g_{\text{Gaia}}$ slightly higher than $\log g_{\text{seis}}$ at lower $\log g$ values. This is consistent with Figure 10 in [Andrae](#)
 276 [et al. \(2023\)](#).

277

6.2. Compared to literature

278 As shown in Figure 13, we compare the distribution of oscillators identified in this work with those reported in
 279 previous studies ([Hon et al. 2021, 2022](#); [Hatt et al. 2023](#); [Zhou et al. 2024](#)) as a function of ν_{max} . In the TESS 2-
 280 minute cadence targets of the southern hemisphere, this work yields the largest number of detected oscillators among
 281 all studies. In addition, this work contributes 2,972 newly identified oscillators that were not reported in the earlier
 282 literature, of which 717 are classified as Type 1. More than half of the new detections fall within the frequency regime
 283 of $\nu_{\text{max}} < 20\mu\text{Hz}$. Among the Type 1 oscillators, 1,920 were not provided with $\Delta\nu$ measurements in previous studies.

284 We compared the asteroseismic parameters derived in this work with those reported in the literature. Figure 14
 285 shows the ν_{max} values for the oscillators common to both samples, with the lower panel presenting the fractional
 286 residuals between the literature values and our measurements. The median, 5th percentile, and 95th percentile of
 287 fractional residuals are -1.9% , -12.4% and 9.7% , respectively. Figure 15 shows the comparison of $\Delta\nu$ for the Type
 288 1 oscillators. The fractional residuals have a median of 0.8% , with the 5th and 95th percentiles at -5.7% and 7.8% ,
 289 respectively.

290 We assessed the consistency between the parameters measured in this work and those reported in previous studies
 291 using the inequality $|Para_{\text{thiswork}} - Para_{\text{literature}}| \leq (error_{\text{thiswork}}^2 + error_{\text{literature}}^2)^{1/2}$, where $Para$ represents either
 292 $\Delta\nu$ or ν_{max} . For $\Delta\nu$, among oscillators for which $\Delta\nu$ values are available both in this work and in [Hon et al. \(2022\)](#),
 293 [Hatt et al. \(2023\)](#), and [Zhou et al. \(2024\)](#), the fractions satisfying this inequality are 48%, 64%, and 82%, respectively.
 294 For ν_{max} , among oscillators in common between this work and [Hon et al. \(2021\)](#), [Hon et al. \(2022\)](#), [Hatt et al. \(2023\)](#),
 295 and [Zhou et al. \(2024\)](#), the corresponding fractions are 77%, 37%, 50%, and 75%, respectively. Overall, the parameters
 296 derived in this work show good agreement with those reported in most previous studies, except for a relatively poorer

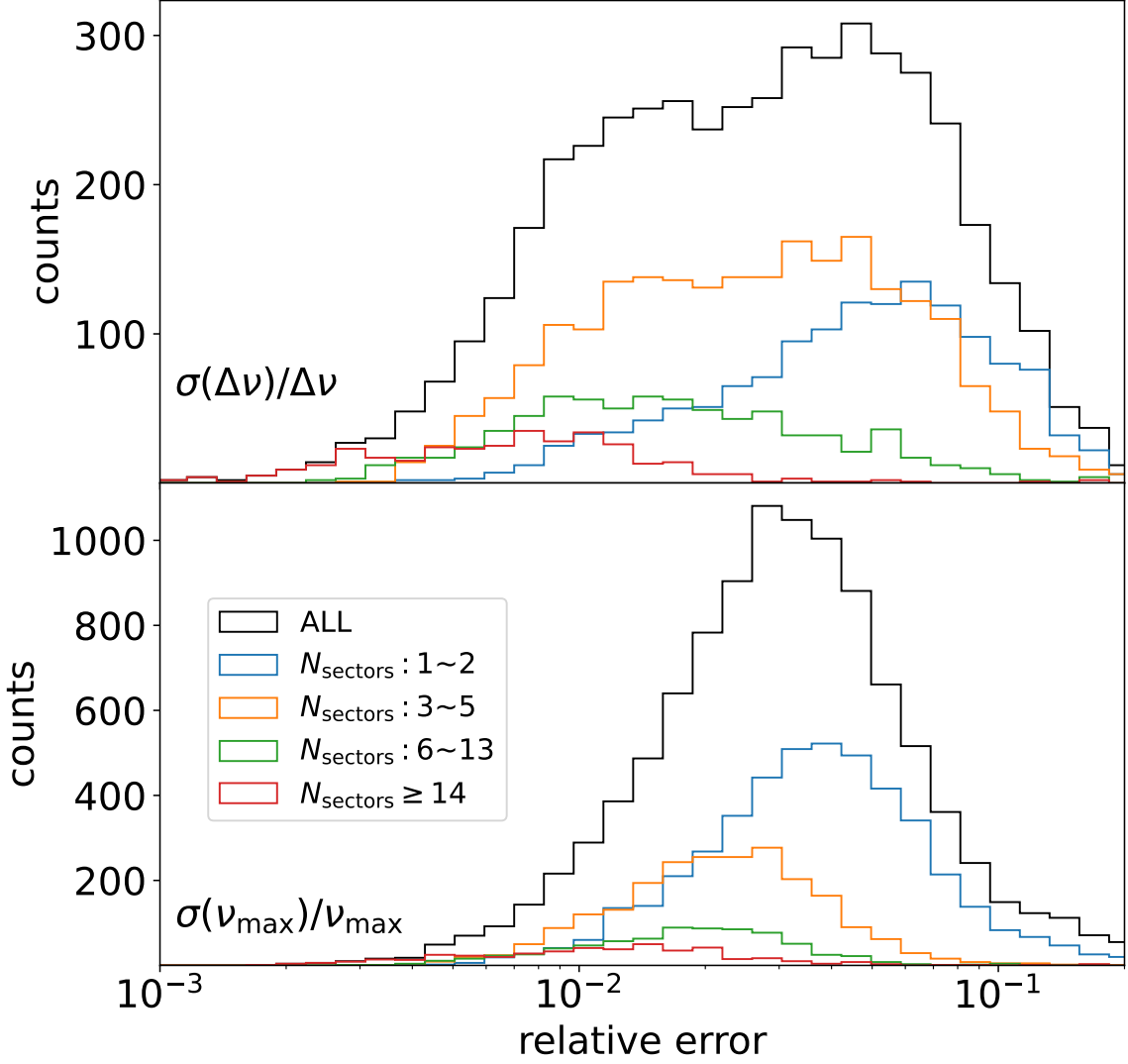


Figure 10. The upper and lower panels present the uncertainty distributions of $\Delta\nu$ and ν_{\max} , respectively. N_{sectors} indicates the number of observing sectors.

297 consistency with the ν_{\max} values from [Hatt et al. \(2023\)](#) and with the parameters from [Hon et al. \(2021\)](#). As shown
 298 in Figures 14 and 15, although the differences between the parameters from [Hon et al. \(2021\)](#) and those obtained in
 299 this work are not large, the consistency metric yields poor consistency. This may be attributed to the fact that stars
 300 observed in continuous viewing zones of TESS benefit from longer effective observing times, leading to smaller formal
 301 uncertainties. In such cases, the estimation of uncertainties may require additional consideration of the frequency
 302 resolution.

303 7. SUMMARY

304 In this work, we present a novel method searching for solar-like oscillators. The method detects excess power
 305 humps by examining the slope of the PSD profile and by applying selection criteria derived from fitting the oscillation
 306 spectra of known solar-like oscillators in the [Hatt et al. \(2023\)](#). Applying this method to the 220,000 TESS 2-minute
 307 targets in the southern hemisphere yielded 16,800 candidates. After visual inspection, we identified 10,548 solar-like
 308 oscillators. We measured ν_{\max} and $\Delta\nu$ using the segmented autocorrelation technique, and assessed the reliability of
 309 the $\Delta\nu$ measurements through the Fourier transform of the autocorrelation function. Based on this assessment, 4,775
 310 oscillators were classified as Type 1 (reliable $\Delta\nu$) and 5,773 as Type 2 (unreliable $\Delta\nu$). We compared the asteroseismic
 311 radii and surface gravities derived from the scaling relations with the radii from the TESS Input Catalog (TIC) and

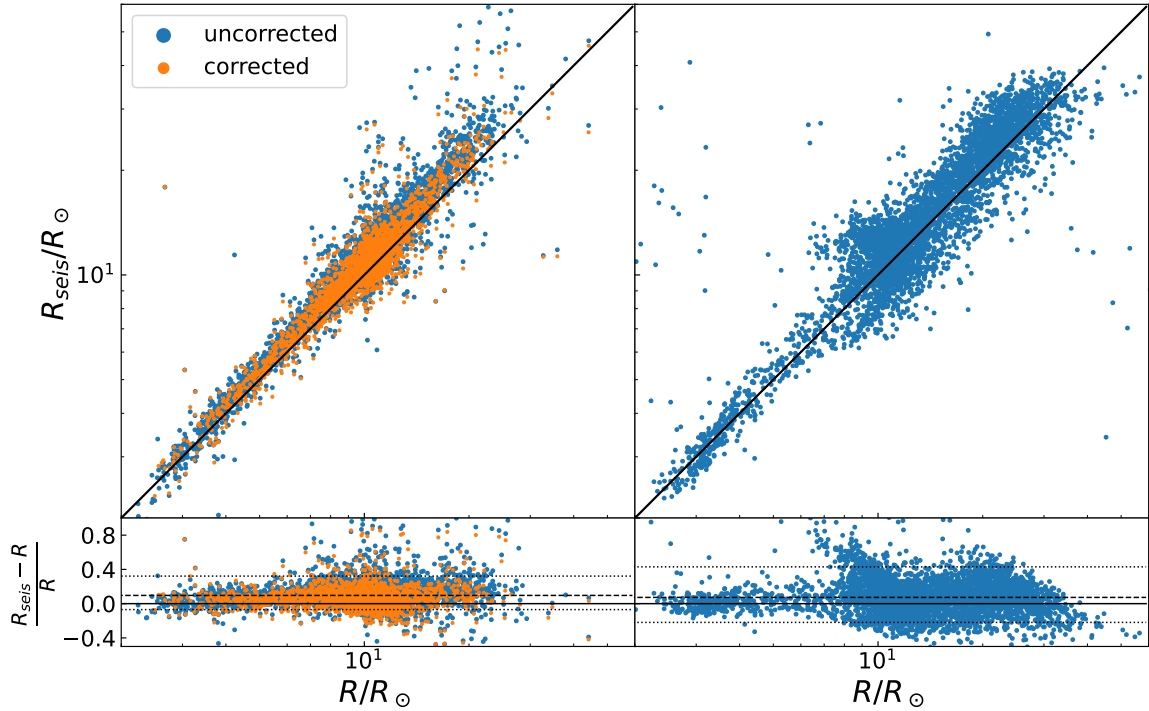


Figure 11. R_{photo} vs. R_{seis} : comparison of radii calculated from the scaling relation and from TESS Input Catalog. The left panel shows the oscillators classified as Type 1, and the right panel shows those classified as Type 2. In the upper panels, the solid lines indicate the 1:1 equality line. The lower panels display the fractional residuals between the two calculated radii. The dashed lines denote the median of the fractional residuals, while the dotted lines indicate 5th percentile and 95th percentile of the fractional residuals, respectively.

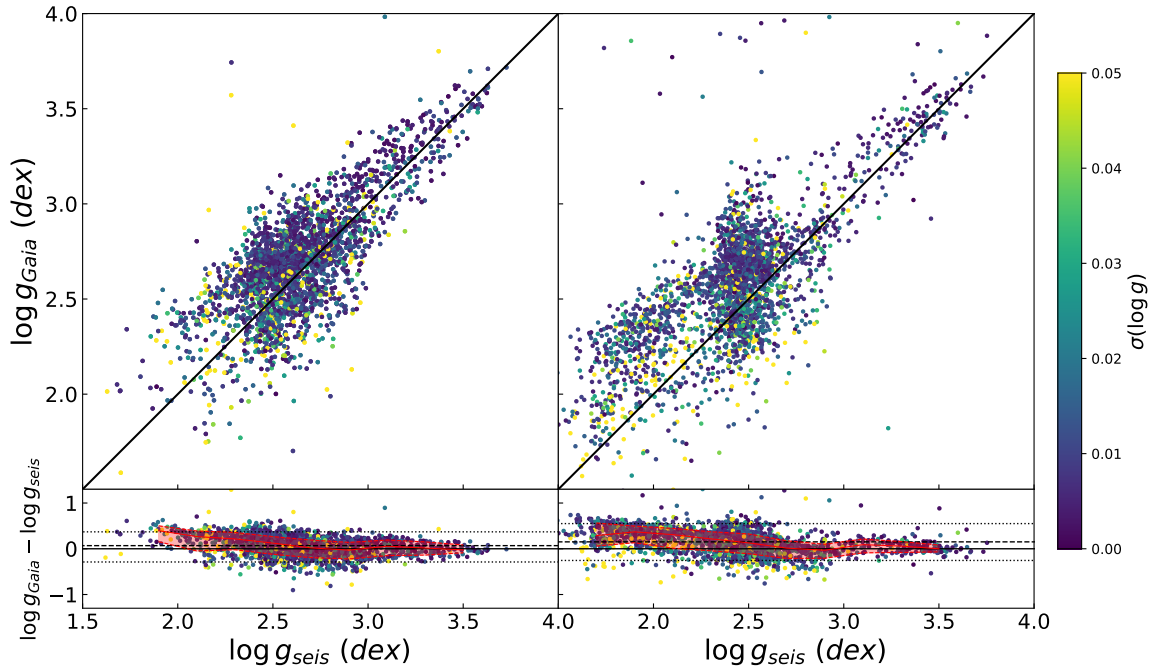


Figure 12. $\log g_{\text{Gaia}}$ vs. $\log g_{\text{seis}}$: A comparison of surface gravity $\log g$ derived from scaling relations and Gaia DR3 data. In the upper panel, the solid lines represent the 1:1 equality line, and the color bar represents the error of $\log g_{\text{Gaia}}$. The lower panels display the residuals of $\log g_{\text{Gaia}} - \log g_{\text{seis}}$. The red shaded area marks the region encompassing 68% of the data within bins of width 0.2.

Table 1. Stellar Global Oscillation Parameters

TIC	T_{eff}	rad	[Fe/H]	$\log g$	$\nu_{\text{max,fit}}$	ν_{max}	$\Delta\nu$	N_{sectors}
	(K)	R_{\odot}			(μHz)	(μHz)	(μHz)	
(1)	(2)	(3)	(4)	(5)	(6)	(7)	(8)	(9)
Type 1								
1608	4799	12.191	-0.0544	2.677	45.01 ± 0.92	47.98 ± 1.77	4.72 ± 0.19	2
13727	5216	3.960			187.97 ± 1.34	190.13 ± 2.17	15.87 ± 0.23	2
70380	4991	10.247			38.50 ± 2.43	41.21 ± 1.52	4.46 ± 0.55	3
80047	4814	6.537	0.0382	2.932	68.02 ± 1.40	70.83 ± 2.64	6.95 ± 0.18	1
89696	4892	8.302	-0.0323	3.015	43.00 ± 0.36	43.29 ± 0.57	4.89 ± 0.55	1
105245	4879	3.979	-0.0617	3.342	274.17 ± 3.1	272.56 ± 2.29	18.53 ± 0.44	3
589906	4305	15.999			16.41 ± 0.32	16.77 ± 0.48	2.06 ± 0.09	2
608932	4945	8.908	-0.1266	2.842	60.90 ± 1.17	61.73 ± 1.51	5.41 ± 0.32	1
612908	4895	5.003	-0.2288	3.196	167.11 ± 1.48	166.39 ± 1.51	13.47 ± 0.21	2
770660	5102	10.749	-0.0399	2.872	63.14 ± 2.68	65.61 ± 2.62	6.01 ± 0.41	2
...								
Type 2								
11001	4510	15.606			17.13 ± 0.63	18.55 ± 0.74		2
74676	4340				16.98 ± 0.38	17.10 ± 0.62		3
92094	4728	10.823	0.1524	2.698	43.01 ± 0.68	46.15 ± 1.41		3
111876	4572	11.330	0.2021	2.556	38.13 ± 0.79	38.63 ± 1.07		3
148113	4348	20.721			10.87 ± 1.88	12.77 ± 0.99		2
152762	4785	10.826			36.78 ± 0.42	39.25 ± 0.97		3
155455	4423	22.478			13.91 ± 0.20	13.84 ± 0.17		4
627296	4668	11.020			29.70 ± 0.67	31.45 ± 1.39		2
683071	4782	10.822			34.65 ± 0.55	36.26 ± 1.09		2
710187	4920	9.339	-0.0268	2.903	83.17 ± 1.24	87.81 ± 2.22		2
...								

NOTE—The data presented in the table is sourced from the TESS Input Catalog, including T_{eff} and radii; [Fe/H] and $\log g$ are sourced from Gaia.

312 the $\log g$ values from Gaia DR3. A systematic offset is found between the asteroseismic radii and those listed in
313 the TIC. After applying the $\Delta\nu$ correction factor of Sharma et al. (2016), the median fractional residual decreases
314 from 9.6% to 5.8%, although a systematic difference remains, suggesting that additional corrections may be required.
315 Compared with previous studies, this work adds 2,972 newly identified TESS oscillators, including 717 high-quality
316 stars classified as Type 1. In addition, the Type 1 sample contains 1,920 oscillators for which no $\Delta\nu$ measurements
317 were provided in earlier studies. Finally, the ν_{max} and $\Delta\nu$ values derived in this study show good agreement with
318 literature measurements, confirming the reliability of the asteroseismic parameters obtained here.

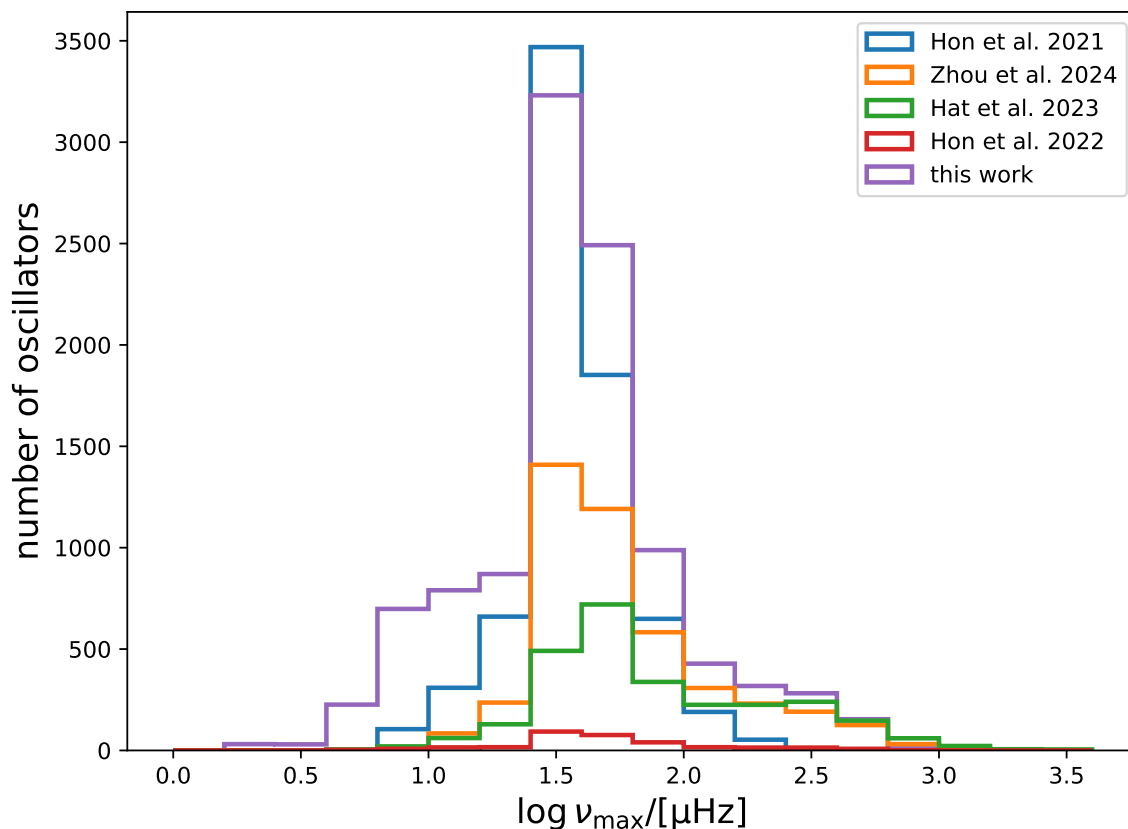


Figure 13. Comparison between the number of oscillators reported in the literature and those detected in this work within the 220,000 target stars analyzed.

319 This work is co-supported from the National Natural Science Foundation of China (Grant No. 12288102), from the
 320 National Key R&D Program of China (Grant No. 2021YFA1600400/2021YFA1600402), and from B-type Strategic
 321 Priority Program of the Chinese Academy of Sciences (Grant No. XDB41000000). The authors also gratefully
 322 acknowledge the supports of NSFC of China (Grant Nos. 12133011 and 12273104), Yunnan Fundamental Research
 323 Projects (Grant No. 202401AS070045), Youth Innovation Promotion Association of Chinese Academy of Sciences,
 324 Ten Thousand Talents Program of Yunnan for Top-notch Young Talents, and the International Centre of Supernovae,
 325 Yunnan Key Laboratory (No. 202302AN360001). H.F.X. acknowledges support from the National Natural Science
 326 Foundation of China (NSFC; No. 12303036) and the Scientific and Technological Innovation Programs of Higher
 327 Education Institutions in Shanxi (STIP; 2025Q032). This work utilized open data from the Transiting Exoplanet
 328 Survey Satellite (TESS) mission and the Gaia mission. The TESS data were provided by NASA and can be accessed
 329 via the MAST archive (<https://archive.stsci.edu/>), while the Gaia data were made available by the European Space
 330 Agency (ESA) and are publicly accessible through the Gaia archive (<https://www.cosmos.esa.int/web/gaia>). The
 331 authors gratefully acknowledge the use of Python and several open-source Python packages, including NumPy (Harris
 332 et al. 2020), SciPy (Virtanen et al. 2020), Matplotlib (Hunter 2007), Astropy (Astropy Collaboration et al. 2022),
 333 Pandas (Wes McKinney 2010) and lightkurve (Lightkurve Collaboration et al. 2018), which were crucial for data
 334 processing, analysis, and visualization. Additionally, the authors thank the developers of TOPCAT (Taylor 2005),
 335 which was used for performing positional cross-matching of stars in this work. The authors would like to thank
 336 ChatGPT, an AI language model developed by OpenAI, for providing assistance with writing, editing, and improving
 337 the clarity of the manuscript.

REFERENCES

- 338 Aerts, C. 2021, *Reviews of Modern Physics*, 93, 015001, doi: [10.1103/RevModPhys.93.015001](https://doi.org/10.1103/RevModPhys.93.015001)
 339
 340 Andrae, R., Fouesneau, M., Sordo, R., et al. 2023, *A&A*,
 341 674, A27, doi: [10.1051/0004-6361/202243462](https://doi.org/10.1051/0004-6361/202243462)

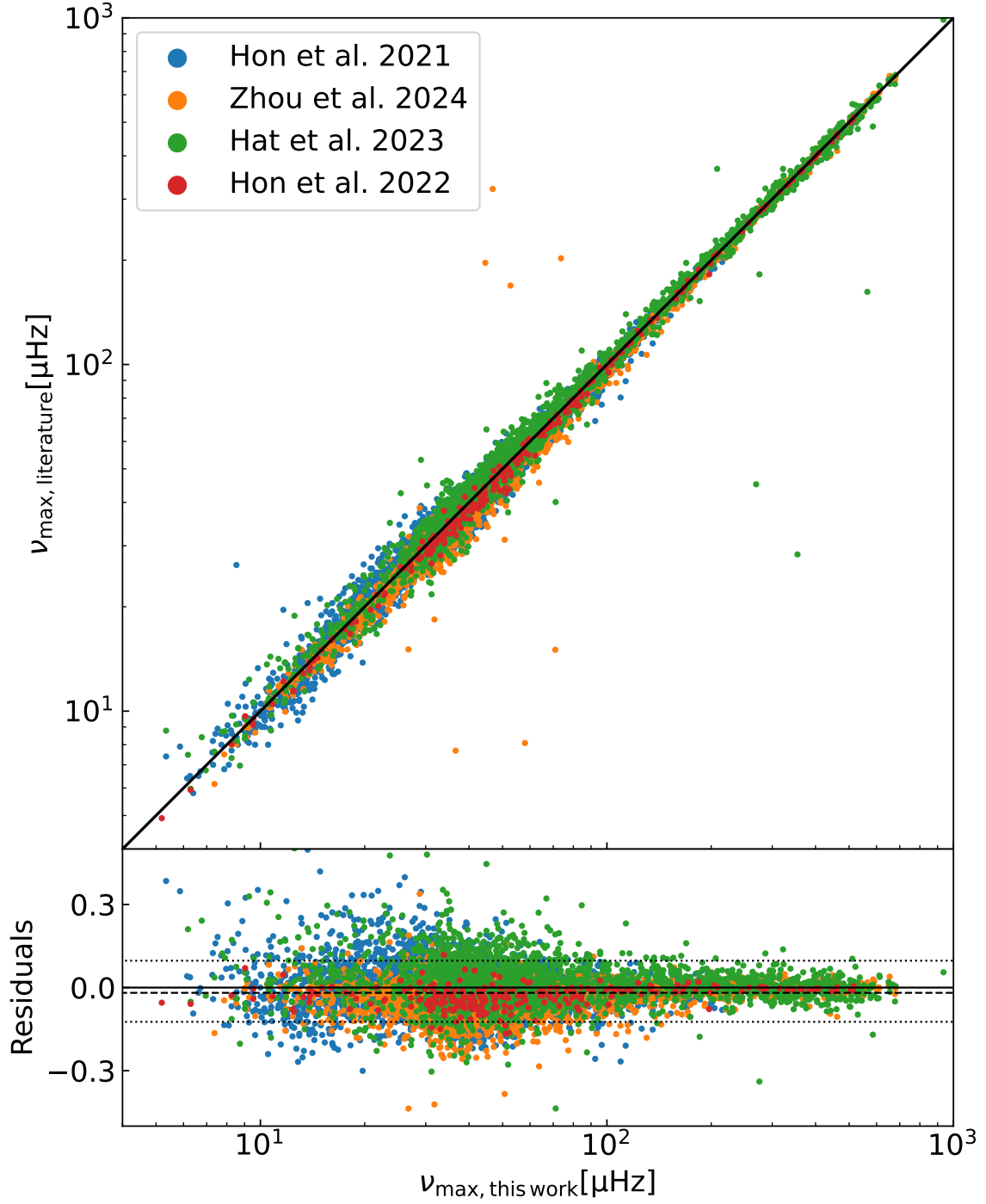


Figure 14. Comparison between the ν_{\max} values reported in the literature and those measured in this work. The lower panels display fractional residuals between ν_{\max} values, calculated as $(\nu_{\max, \text{literature}} - \nu_{\max, \text{this work}}) / \nu_{\max, \text{this work}}$. **The dashed lines denote the median of the fractional residuals, while the dotted lines indicate 5th percentile and 95th percentile of the fractional residuals, respectively.**

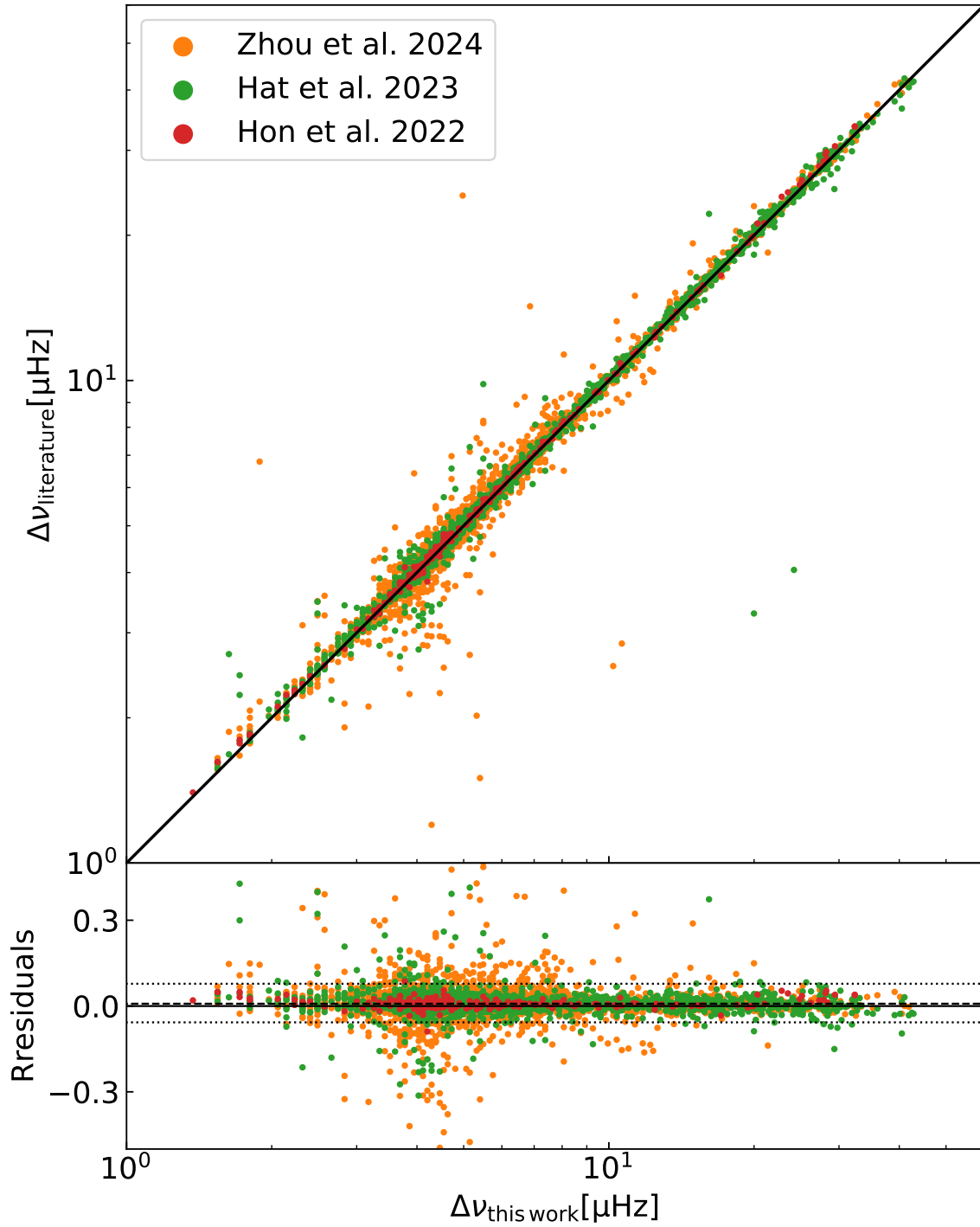


Figure 15. Comparison between the $\Delta\nu$ values reported in the literature and those measured in this work for oscillators classified as Type 1. The lower panels display the fractional residuals of $\Delta\nu$, calculated as $(\Delta\nu_{\text{literature}} - \Delta\nu_{\text{this work}})/\Delta\nu_{\text{this work}}$. The dashed lines denote the median of the fractional residuals, while the dotted lines indicate 5th percentile and 95th percentile of the fractional residuals, respectively.

- 342 Astropy Collaboration, Price-Whelan, A. M., Lim, P. L.,
343 et al. 2022, *ApJ*, 935, 167, doi: [10.3847/1538-4357/ac7c74](https://doi.org/10.3847/1538-4357/ac7c74)
- 344 Baglin, A., Auvergne, M., Boissard, L., et al. 2006, in 36th
345 COSPAR Scientific Assembly, Vol. 36, 3749
- 346 Bedding, T. R., & Kjeldsen, H. 2022, *Research Notes of the*
347 *American Astronomical Society*, 6, 202,
348 doi: [10.3847/2515-5172/ac8f94](https://doi.org/10.3847/2515-5172/ac8f94)
- 349 Bellinger, E. P. 2019, *MNRAS*, 486, 4612,
350 doi: [10.1093/mnras/stz714](https://doi.org/10.1093/mnras/stz714)
- 351 Bellinger, E. P., Hekker, S., Angelou, G. C., Stokholm, A.,
352 & Basu, S. 2019, *A&A*, 622, A130,
353 doi: [10.1051/0004-6361/201834461](https://doi.org/10.1051/0004-6361/201834461)
- 354 Berger, T. A., Huber, D., Gaidos, E., & van Saders, J. L.
355 2018, *ApJ*, 866, 99, doi: [10.3847/1538-4357/aada83](https://doi.org/10.3847/1538-4357/aada83)
- 356 Borucki, W. J., Koch, D., Basri, G., et al. 2010, *Science*,
357 327, 977, doi: [10.1126/science.1185402](https://doi.org/10.1126/science.1185402)
- 358 Bovy, J., Rix, H.-W., Green, G. M., Schlafly, E. F., &
359 Finkbeiner, D. P. 2016, *ApJ*, 818, 130,
360 doi: [10.3847/0004-637X/818/2/130](https://doi.org/10.3847/0004-637X/818/2/130)
- 361 Ginsburg, A., Sipőcz, B. M., Brasseur, C. E., et al. 2019,
362 *AJ*, 157, 98, doi: [10.3847/1538-3881/aafc33](https://doi.org/10.3847/1538-3881/aafc33)
- 363 Harris, C. R., Millman, K. J., van der Walt, S. J., et al.
364 2020, *Nature*, 585, 357, doi: [10.1038/s41586-020-2649-2](https://doi.org/10.1038/s41586-020-2649-2)
- 365 Harvey, J. 1985, in *ESA Special Publication*, Vol. 235,
366 *Future Missions in Solar, Heliospheric & Space Plasma*
367 *Physics*, ed. E. Rolfe & B. Battrick, 199
- 368 Hatt, E., Nielsen, M. B., Chaplin, W. J., et al. 2023, *A&A*,
369 669, A67, doi: [10.1051/0004-6361/202244579](https://doi.org/10.1051/0004-6361/202244579)
- 370 Hekker, S. 2020, *Frontiers in Astronomy and Space*
371 *Sciences*, 7, 3, doi: [10.3389/fspas.2020.00003](https://doi.org/10.3389/fspas.2020.00003)
- 372 Hekker, S., Kallinger, T., Baudin, F., et al. 2009, *A&A*,
373 506, 465, doi: [10.1051/0004-6361/200911858](https://doi.org/10.1051/0004-6361/200911858)
- 374 Hekker, S., Gilliland, R. L., Elsworth, Y., et al. 2011,
375 *MNRAS*, 414, 2594,
376 doi: [10.1111/j.1365-2966.2011.18574.x](https://doi.org/10.1111/j.1365-2966.2011.18574.x)
- 377 Hon, M., Kuszewicz, J. S., Huber, D., Stello, D., & Reyes,
378 C. 2022, *AJ*, 164, 135, doi: [10.3847/1538-3881/ac8931](https://doi.org/10.3847/1538-3881/ac8931)
- 379 Hon, M., Stello, D., García, R. A., et al. 2019, *MNRAS*,
380 485, 5616, doi: [10.1093/mnras/stz622](https://doi.org/10.1093/mnras/stz622)
- 381 Hon, M., Huber, D., Kuszewicz, J. S., et al. 2021, *ApJ*,
382 919, 131, doi: [10.3847/1538-4357/ac14b1](https://doi.org/10.3847/1538-4357/ac14b1)
- 383 Howell, S. B., Sobek, C., Haas, M., et al. 2014, *PASP*, 126,
384 398, doi: [10.1086/676406](https://doi.org/10.1086/676406)
- 385 Huber, D., Stello, D., Bedding, T. R., et al. 2009,
386 *Communications in Asteroseismology*, 160, 74,
387 doi: [10.48550/arXiv.0910.2764](https://doi.org/10.48550/arXiv.0910.2764)
- 388 Huber, D., Bedding, T. R., Stello, D., et al. 2011, *ApJ*, 743,
389 143, doi: [10.1088/0004-637X/743/2/143](https://doi.org/10.1088/0004-637X/743/2/143)
- 390 Huber, D., Silva Aguirre, V., Matthews, J. M., et al. 2014,
391 *ApJS*, 211, 2, doi: [10.1088/0067-0049/211/1/2](https://doi.org/10.1088/0067-0049/211/1/2)
- 392 Hunter, J. D. 2007, *Computing in Science & Engineering*, 9,
393 90, doi: [10.1109/MCSE.2007.55](https://doi.org/10.1109/MCSE.2007.55)
- 394 Jiang, C., Jiang, B. W., Christensen-Dalsgaard, J., et al.
395 2011, *ApJ*, 742, 120, doi: [10.1088/0004-637X/742/2/120](https://doi.org/10.1088/0004-637X/742/2/120)
- 396 Joshi, S., & Joshi, Y. C. 2015, *Journal of Astrophysics and*
397 *Astronomy*, 36, 33, doi: [10.1007/s12036-015-9327-z](https://doi.org/10.1007/s12036-015-9327-z)
- 398 Kallinger, T., Weiss, W. W., Barban, C., et al. 2010a,
399 *A&A*, 509, A77, doi: [10.1051/0004-6361/200811437](https://doi.org/10.1051/0004-6361/200811437)
- 400 Kallinger, T., Mosser, B., Hekker, S., et al. 2010b, *A&A*,
401 522, A1, doi: [10.1051/0004-6361/201015263](https://doi.org/10.1051/0004-6361/201015263)
- 402 Kjeldsen, H., & Bedding, T. R. 1995, *A&A*, 293, 87,
403 doi: [10.48550/arXiv.astro-ph/9403015](https://doi.org/10.48550/arXiv.astro-ph/9403015)
- 404 Li, T., Li, Y., Bi, S., et al. 2022, *ApJ*, 927, 167,
405 doi: [10.3847/1538-4357/ac4fbf](https://doi.org/10.3847/1538-4357/ac4fbf)
- 406 Lightkurve Collaboration, Cardoso, J. V. d. M., Hedges, C.,
407 et al. 2018, *Lightkurve: Kepler and TESS time series*
408 *analysis in Python*, *Astrophysics Source Code Library*.
409 <http://ascl.net/1812.013>
- 410 Lomb, N. R. 1976, *Ap&SS*, 39, 447,
411 doi: [10.1007/BF00648343](https://doi.org/10.1007/BF00648343)
- 412 Mathur, S., García, R. A., Huber, D., et al. 2016, *ApJ*, 827,
413 50, doi: [10.3847/0004-637X/827/1/50](https://doi.org/10.3847/0004-637X/827/1/50)
- 414 Mosser, B., Belkacem, K., Goupil, M. J., et al. 2010, *A&A*,
415 517, A22, doi: [10.1051/0004-6361/201014036](https://doi.org/10.1051/0004-6361/201014036)
- 416 Nielsen, M. B., Hatt, E., Chaplin, W. J., Ball, W. H., &
417 Davies, G. R. 2022, *A&A*, 663, A51,
418 doi: [10.1051/0004-6361/202243064](https://doi.org/10.1051/0004-6361/202243064)
- 419 Ricker, G. R., Winn, J. N., Vanderspek, R., et al. 2015,
420 *Journal of Astronomical Telescopes, Instruments, and*
421 *Systems*, 1, 014003, doi: [10.1117/1.JATIS.1.1.014003](https://doi.org/10.1117/1.JATIS.1.1.014003)
- 422 Scargle, J. D. 1982, *ApJ*, 263, 835, doi: [10.1086/160554](https://doi.org/10.1086/160554)
- 423 Sharma, S., Stello, D., Bland-Hawthorn, J., Huber, D., &
424 Bedding, T. R. 2016, *ApJ*, 822, 15,
425 doi: [10.3847/0004-637X/822/1/15](https://doi.org/10.3847/0004-637X/822/1/15)
- 426 Silva Aguirre, V., Stello, D., Stokholm, A., et al. 2020,
427 *ApJL*, 889, L34, doi: [10.3847/2041-8213/ab6443](https://doi.org/10.3847/2041-8213/ab6443)
- 428 Stassun, K. G., Oelkers, R. J., Pepper, J., et al. 2018, *AJ*,
429 156, 102, doi: [10.3847/1538-3881/aad050](https://doi.org/10.3847/1538-3881/aad050)
- 430 Stassun, K. G., Oelkers, R. J., Paegert, M., et al. 2019, *AJ*,
431 158, 138, doi: [10.3847/1538-3881/ab3467](https://doi.org/10.3847/1538-3881/ab3467)
- 432 Stello, D., Chaplin, W. J., Bruntt, H., et al. 2009, *ApJ*, 700,
433 1589, doi: [10.1088/0004-637X/700/2/1589](https://doi.org/10.1088/0004-637X/700/2/1589)
- 434 Stello, D., Huber, D., Bedding, T. R., et al. 2013, *ApJL*,
435 765, L41, doi: [10.1088/2041-8205/765/2/L41](https://doi.org/10.1088/2041-8205/765/2/L41)
- 436 Stello, D., Zinn, J., Elsworth, Y., et al. 2017, *ApJ*, 835, 83,
437 doi: [10.3847/1538-4357/835/1/83](https://doi.org/10.3847/1538-4357/835/1/83)
- 438 Stello, D., Saunders, N., Grunblatt, S., et al. 2022,
439 *MNRAS*, 512, 1677, doi: [10.1093/mnras/stac414](https://doi.org/10.1093/mnras/stac414)

- 440 Taylor, M. B. 2005, in *Astronomical Society of the Pacific*
441 *Conference Series*, Vol. 347, *Astronomical Data Analysis*
442 *Software and Systems XIV*, ed. P. Shopbell, M. Britton,
443 & R. Ebert, 29
- 444 VanderPlas, J. T. 2018, *ApJS*, 236, 16,
445 doi: [10.3847/1538-4365/aab766](https://doi.org/10.3847/1538-4365/aab766)
- 446 Viani, L. S., Basu, S., Chaplin, W. J., Davies, G. R., &
447 Elsworth, Y. 2017, *ApJ*, 843, 11,
448 doi: [10.3847/1538-4357/aa729c](https://doi.org/10.3847/1538-4357/aa729c)
- 449 Virtanen, P., Gommers, R., Oliphant, T. E., et al. 2020,
450 *Nature Methods*, 17, 261, doi: [10.1038/s41592-019-0686-2](https://doi.org/10.1038/s41592-019-0686-2)
- 451 Wes McKinney. 2010, in *Proceedings of the 9th Python in*
452 *Science Conference*, ed. Stéfan van der Walt & Jarrod
453 Millman, 56 – 61, doi: [10.25080/Majora-92bf1922-00a](https://doi.org/10.25080/Majora-92bf1922-00a)
- 454 White, T. R., Bedding, T. R., Stello, D., et al. 2011, *ApJ*,
455 743, 161, doi: [10.1088/0004-637X/743/2/161](https://doi.org/10.1088/0004-637X/743/2/161)
- 456 Wu, T., Li, Y., & Hekker, S. 2014, *ApJ*, 781, 44,
457 doi: [10.1088/0004-637X/781/1/44](https://doi.org/10.1088/0004-637X/781/1/44)
- 458 Yu, J., Huber, D., Bedding, T. R., et al. 2018, *ApJS*, 236,
459 42, doi: [10.3847/1538-4365/aaaf74](https://doi.org/10.3847/1538-4365/aaaf74)
- 460 —. 2016, *MNRAS*, 463, 1297, doi: [10.1093/mnras/stw2074](https://doi.org/10.1093/mnras/stw2074)
- 461 Zhou, J., Bi, S., Yu, J., et al. 2024, *ApJS*, 271, 17,
462 doi: [10.3847/1538-4365/ad18db](https://doi.org/10.3847/1538-4365/ad18db)